

1 INTRODUCTION

2 Above Earth's atmosphere are the a pair of Van Allen radiation belts, a complex  
3 and dynamic plasma environment that affects our technology-driven society. These  
4 effects include: a higher radiation dose for astronauts and cosmonauts, higher chance  
5 of spacecraft failure due to single event upsets that can lead to catastrophic latchups,  
6 degradation of silicon (changing the silicon doping) from an extended radiation dose  
7 that can degrade a transistor to the point where it no longer function as a switch,  
8 and the degradation of the ozone layer due to the chemical production of  $\text{NO}_X$  and  
9  $\text{HO}_X$  molecules. With these effects in mind, it is no surprise that the radiation belts  
10 have been extensively studied since their discovery in the 1960s.

11 One natural phenomenon in the radiation belts that has been a topic of interest  
12 in the space physics community is wave-particle interactions that, as we will explore  
13 throughout this dissertation, can accelerate particles to very high energies (e.g.  $\approx$   
14 MeV for electrons) and scatter them into the atmosphere.

15 The goal of this dissertation is to study the wave-particle scattering mechanism  
16 that scatters electron microbursts. Electron microbursts, henceforth referred to  
17 as microbursts, are typically observed by low Earth orbiting spacecraft, sounding  
18 rockets, and high altitude balloons as a sub-second impulse of electrons. Some of  
19 the most intense microbursts are observed as a 10 to 100 fold increase of electrons  
20 (for example see Fig. 7 in Blake et al. (1996)). Since they were first reported by  
21 Anderson and Milton (1964), the short microburst duration and their impulsive nature  
22 have compelled countless researchers to understand their properties and the physical  
23 mechanism(s) that create microbursts. Microbursts are widely believed to be created  
24 by wave-particle scattering between a plasma wave called whistler mode chorus  
25 and outer radiation belt electrons, although many details regarding the scattering

<sup>26</sup> mechanism are unconstrained or unknown.

<sup>27</sup> This chapter serves as an introduction to the physics of charged particles, plasma  
<sup>28</sup> waves, and the wave-particle interactions in Earth's magnetosphere. We will first  
<sup>29</sup> derive the motion of individual charged particles in Earth's electric and magnetic  
<sup>30</sup> fields. Then we will cover how various groups of charged particles coalesce to form  
<sup>31</sup> the major particle populations in the magnetosphere. Then, we will cover the various  
<sup>32</sup> mechanisms that accelerate particles in the magnetosphere. Lastly, we will review  
<sup>33</sup> the basics of microbursts as a jumping-off point for the rest of the dissertation.

<sup>34</sup> Charged Particle Motion in Electric and Magnetic Fields

A charged particle trapped in the magnetosphere will experience three types of periodic motion in Earth's nearly dipolar magnetic field. The three motions are ultimately due to the Lorentz force that a particle of momentum  $\vec{p}$ , charge  $q$ , and velocity  $\vec{v}$  experiences in an electric field  $\vec{E}$  and magnetic field  $\vec{B}$  and is given by

$$\frac{d\vec{p}}{dt} = q(\vec{E} + \vec{v} \times \vec{B}). \quad (1.1)$$

<sup>35</sup> In the magnetosphere, the three periodic motions, in decreasing frequency, are  
<sup>36</sup> gyration, bounce, and drift and are schematically shown in Fig. 1.1. Each of periodic  
<sup>37</sup> these motions have a corresponding conserved quantity i.e. an adiabatic invariant.

The highest frequency periodic motion is gyration about a magnetic field of magnitude  $B$ . This motion is circular with a Larmor radius of

$$r = \frac{mv_{\perp}}{|q|B} \quad (1.2)$$

where  $m$  is the mass and  $v_{\perp}$  the particle's velocity perpendicular to  $\vec{B}$ . This motion

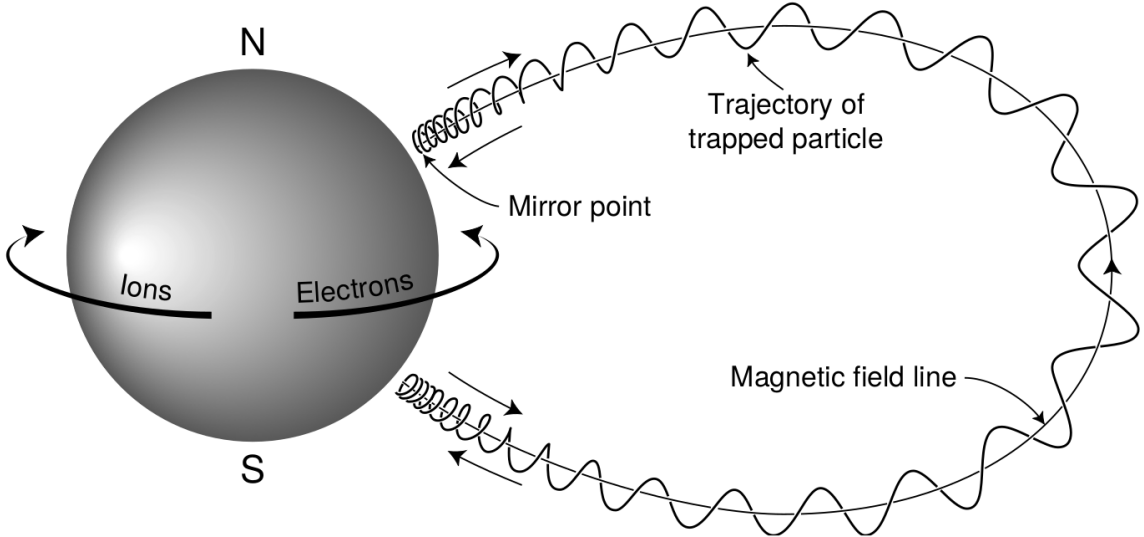


Figure 1.1: The three periodic motions of charged particles in Earth's dipole magnetic field. These motions are: gyration about the magnetic field line, bounce motion between the magnetic poles, and azimuthal drift around the Earth. Figure from (Baumjohann and Treumann, 1997).

has a corresponding gyrofrequency

$$\Omega = \frac{|q|B}{m} \quad (1.3)$$

in units of radians/second. Inside the radiation belts the electron gyrofrequency,  $\Omega_e$  is on the order of a kHz. The corresponding adiabatic invariant is found by integrating the particle's canonical momentum around the particle's path of gyration

$$J_i = \oint (\vec{p} + q\vec{A}) \cdot d\vec{l} \quad (1.4)$$

<sup>38</sup> where  $J_i$  is the  $i^{th}$  adiabatic invariant and  $\vec{A}$  is the magnetic vector potential. This  
<sup>39</sup> integral is carried out by integrating the first term over the circumference of the gyro  
<sup>40</sup> orbit and integrating the second term using Stokes theorem to calculate the magnetic  
<sup>41</sup> flux enclosed by the gyro orbit. The gyration invariant is then  $J_1 \sim v_{\perp}^2/B$ , which is

<sup>42</sup> conserved when the frequency,  $\omega$  of a force acting on the gyrating electron satisfies  
<sup>43</sup>  $\omega \ll \Omega_e$ .

<sup>44</sup> The second highest frequency periodic motion is bouncing due to a parallel  
<sup>45</sup> gradient in  $\vec{B}$ . This periodic motion naturally arises in the magnetosphere because  
<sup>46</sup> Earth's magnetic field is stronger near the poles, and artificially in the laboratory  
<sup>47</sup> in magnetic bottle machines. To understand this motion we first we need to define  
<sup>48</sup> the concept of pitch angle  $\alpha$  as the angle between  $\vec{B}$  and  $\vec{v}$  which is schematically  
<sup>49</sup> shown in Fig. 1.2a. The pitch angle relates  $v$  with  $v_{\perp}$ , and  $v_{\parallel}$  (the component of the  
<sup>50</sup> particles velocity parallel to  $\vec{B}$ ). As shown in 1.2b and c, a smaller (larger)  $\alpha$  will  
<sup>51</sup> increase (decrease) the distance that the charged particle travels parallel to  $\vec{B}$ , during  
<sup>52</sup> one gyration.

Assuming the particle's kinetic energy is conserved, the conservation of  $J_1$  implies that given a particle's  $v_{\perp}(0)$  and  $B(0)$  at the magnetic equator (where Earth's magnetic field is usually at a minimum), we can calculate its  $v_{\perp}(s)$  along the particle's path  $s$  by calculating  $B(s)$  from magnetic field models. The particle's perpendicular velocity is then related via

$$\frac{v_{\perp}^2(0)}{B(0)} = \frac{v_{\perp}^2(s)}{B(s)} \quad (1.5)$$

<sup>53</sup> which can be rewritten as

$$\frac{v^2 \sin^2 \alpha(0)}{B(0)} = \frac{v^2 - v_{\parallel}^2(s)}{B(s)} \quad (1.6)$$

<sup>54</sup> and re-arranged to solve for  $v_{\parallel}(s)$

$$v_{\parallel}(s) = v \sqrt{1 - \frac{B(s)}{B(0)} \sin^2 \alpha(0)} \quad (1.7)$$

<sup>55</sup> which will tend towards 0 when the second term in the radical approaches 1.

56        The location where  $v_{||}(s) = 0$  is called the mirror point and is where a particle  
 57   reverses direction. Since Earth's magnetic field is stronger towards the poles, the  
 58   mirroring particle will execute periodic bounce motion between its two mirror points  
 59   in the northern and southern hemispheres. The corresponding adiabatic invariant,  $J_2$   
 60   is

$$J_2 = \oint p_{||} ds \quad (1.8)$$

where  $ds$  describes the particle path between the mirror points in the northern and southern hemispheres (see Fig. 1.1).  $J_2$  is found by substituting Eq. 1.7 into Eq. 1.8 and defining the magnetic field strength at the mirror points as  $B_m$  where  $\alpha(m) = 90^\circ$ .

The  $J_2$  integral can be written as

$$J_2 = 2p \int_{m_n}^{m_s} \sqrt{1 - \frac{B(s)}{B(m)}} ds \quad (1.9)$$

61   where  $m_n$  and  $m_s$  are the northern and southern mirror points, respectively. The  
 62   bounce period can be estimated (e.g. Baumjohann and Treumann, 1997) to be

$$t_b \approx \frac{LR_e}{\sqrt{W/m}} (3.7 - 1.6 \sin \alpha(0)) \quad (1.10)$$

63   where  $L$  is the  $L$ -shell which describes the distance from the Earth's center to the  
 64   location where a particular magnetic field line crosses the magnetic equator, in units  
 65   of Earth radii,  $R_e$ .  $W$  is the particle's kinetic energy. As with gyration, the particle  
 66   will bounce between the mirror points as long as  $\omega \ll \Omega_b$ , where  $\Omega_b$  is the bounce  
 67   frequency.

68        At this stage it is instructional to introduce the notion of the loss cone pitch  
 69   angle,  $\alpha_L$ . A particle with  $\alpha \leq \alpha_L$  will mirror at or below  $\approx 100$  km altitude in

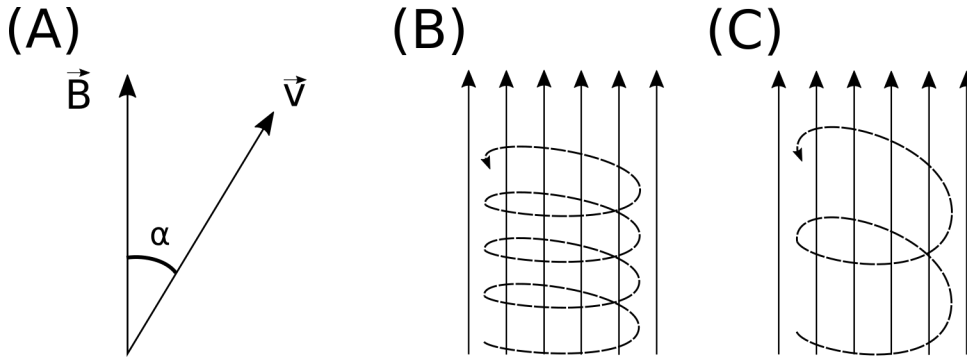


Figure 1.2: Charged particle motion in a uniform magnetic field  $\vec{B}$ . Panel (A) shows the geometry defining the pitch angle,  $\alpha$ . Panel (B) and (C) show two helical electron trajectories with dashed lines assuming a large and small  $\alpha$  (corresponding to a small and large parallel velocity  $v_{||}$ ), respectively.

70 the atmosphere. A charged particle gyrating at those altitudes will encounter and  
71 Coulomb scatter with the dense atmosphere and be lost from the magnetosphere.

72 The slowest periodic motion experienced by charged particles in Earth's mag-  
73 netic field is azimuthal drift around the Earth. This drift results from a combination of  
74 a radial gradient in  $\vec{B}$  and the curvature of the magnetic field. The radial gradient drift  
75 arises because Earth's magnetic field is stronger near the Earth where the particle's  
76 gyroradius radius of curvature is smaller as it gyrates towards stronger magnetic field,  
77 and larger when it gyrates outward. The overall effect is the particle gyro orbit does  
78 not close on itself and negatively charged particles drift east and positively charged  
79 particles drift west. The radial gradient drift is enhanced by the centrifugal force that  
80 a particle experiences as it bounces along the curved field lines. The drift adiabatic  
81 invariant,  $J_3$  is found by integrating Eq. 1.4 over the complete particle orbit around  
82 the Earth. The shape of this drift orbit is otherwise known as a drift shell. For  $J_3$ ,  
83 the first term is negligible and the second term is the magnetic flux enclosed by the  
84 drift shell,  $\Phi_m$  i.e.  $J_3 \sim \Phi_m$ .

85 Figure 1.3 from Schulz and Lanzerotti (1974) shows contours of the gyration,

<sup>86</sup> bounce, and drift frequencies for electrons and protons in Earth's dipole magnetic  
<sup>87</sup> field.

Up until now we have considered the three periodic motions due Earth's magnetic field and the absence of electric fields. If  $\vec{E}$  is present, a particle's center of gyration i.e., averaged position of the particle over a gyration, will drift with a velocity perpendicular to both  $\vec{E}$  and  $\vec{B}$ . The drift velocity can be solved directly from Eq. 1.1 and is

$$\vec{v}_E = \frac{\vec{E} \times \vec{B}}{B^2}. \quad (1.11)$$

<sup>88</sup> Lastly, for more detailed derivations of these motions, see the following texts:  
<sup>89</sup> Baumjohann and Treumann (1997); Schulz and Lanzerotti (1974); Tsurutani and  
<sup>90</sup> Lakhina (1997).

## <sup>91</sup> Particle Populations and Their Interractions in the Magnetosphere

<sup>92</sup> Now that we have looked at the dynamics of single-particle motion in electric  
<sup>93</sup> and magnetic fields, we will briefly tour the various macroscopic populations in the  
<sup>94</sup> magnetosphere that are illustrated in Fig. 1.4.

<sup>95</sup> The sun and its solar wind are ultimately the source of energy input into the  
<sup>96</sup> magnetosphere. The solar wind at Earth's orbit is a plasma traveling at supersonic  
<sup>97</sup> speeds with an embedded interplanetary magnetic field (IMF). When the solar wind  
<sup>98</sup> encounters Earth's magnetic field, the plasma can not easily penetrate into the  
<sup>99</sup> magnetosphere because the plasma is frozen-in on magnetic field lines. Thus the  
<sup>100</sup> plasma and its magnetic field drapes around the magnetosphere forming a cavity in  
<sup>101</sup> the solar wind that is roughly shaped as shown in Fig. 1.4. Because the solar wind  
<sup>102</sup> is supersonic at 1 AU, a bow shock exists upstream of the magnetosphere. The solar  
<sup>103</sup> wind plasma, after it is shocked by the bow shock, flows around the magnetosphere

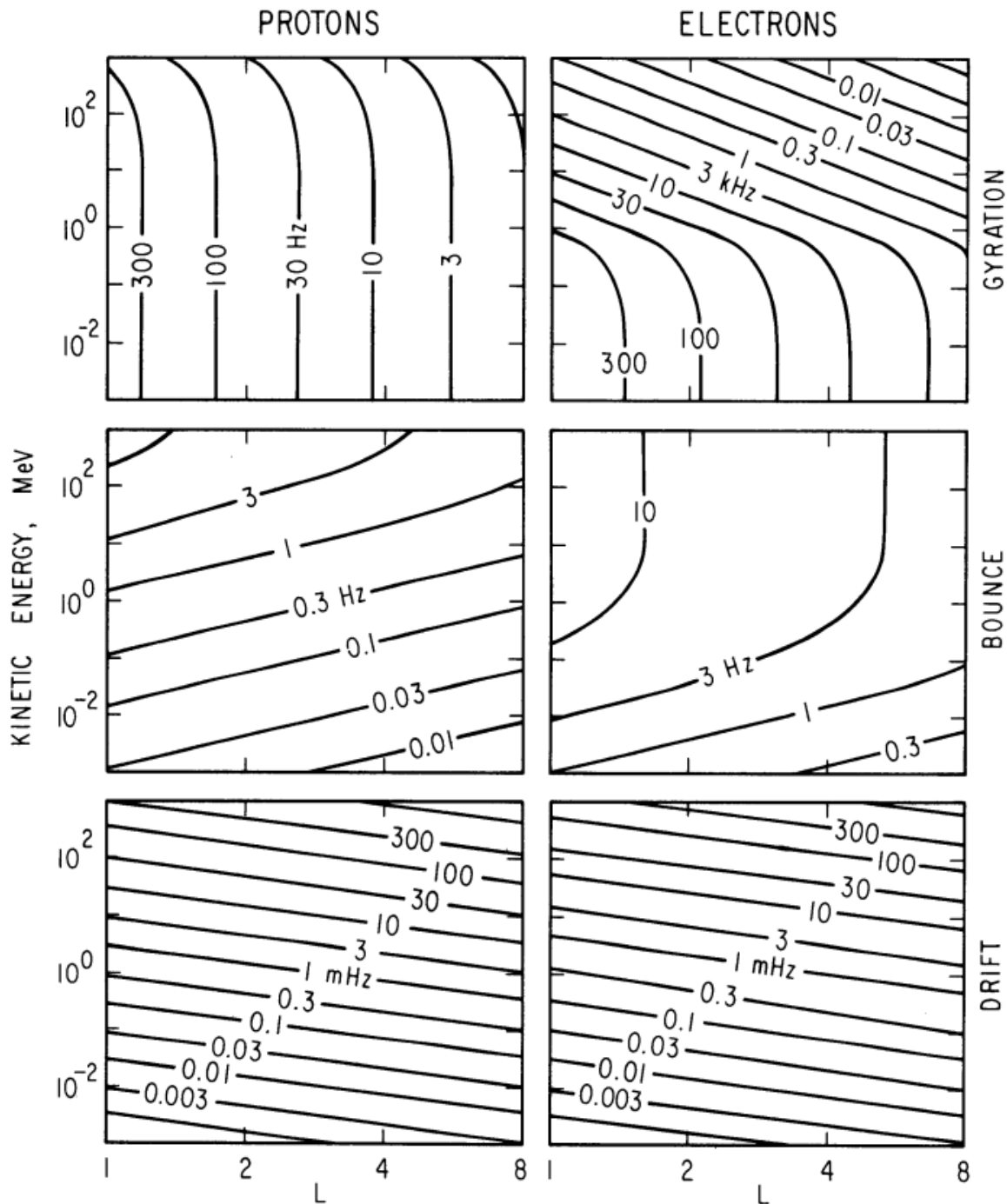


Figure 1.3: Contours of constant gyration, bounce, and drift frequencies for electrons and protons in a dipole field. Figure from Schulz and Lanzerotti (1974).

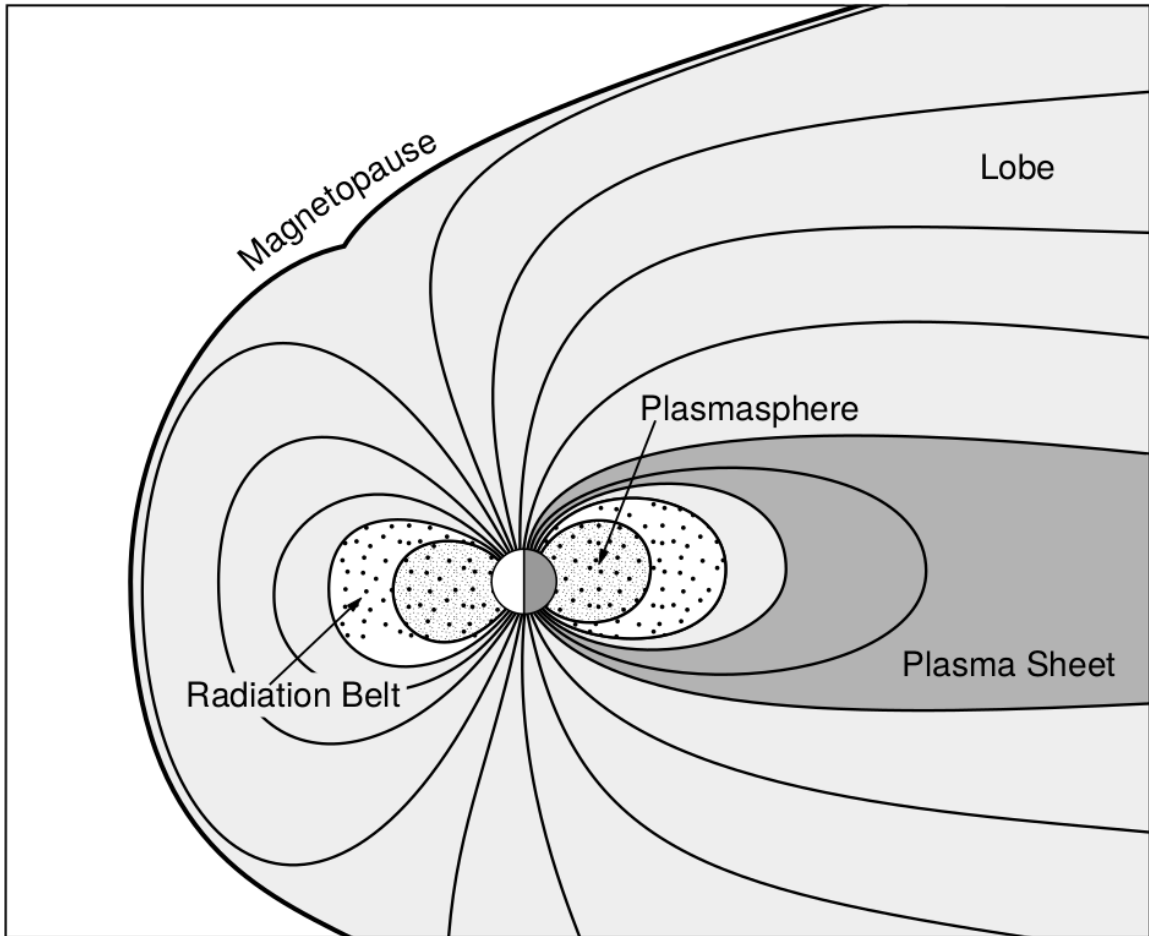


Figure 1.4: Macroscopic structures in the inner magnetosphere most relevant to this dissertation. The plasmasphere, and the radiation belts are shown and ring current is co-located there as well. Figure from Baumjohann and Treumann (1997).

104 inside the magnetosheath. The surface where the solar wind ram pressure and Earth's  
 105 magnetic pressure balance is termed the magnetopause, which can be thought of as  
 106 a boundary between the solar wind's and Earth's plasma environments. This is  
 107 a slightly naive description of the magnetopause, but is nonetheless an instructive  
 108 conceptual picture. The shocked plasma then flows past the Earth where it shapes  
 109 the magnetotail. In the magnetotail the solar wind magnetic pressure balances Earth's  
 110 magnetic field pressure in the lobes. The magnetotail extends on the order of 100  
 111  $R_E$  downstream of Earth, and the tailward stretching of magnetic field lines creates  
 112 the plasma sheet which exists in the region of low magnetic field strength near the  
 113 magnetic equator (e.g. Eastwood et al., 2015).

114 Populations in the Inner Magnetosphere

115 Closer to Earth, where the magnetic field is largely dipolar, are three plasma  
 116 populations that comprise the inner magnetosphere: the plasmasphere, the ring  
 117 current, and the radiation belts. Before we describe these three particle populations  
 118 in detail, we will first introduce the coordinate system that most naturally describes  
 119 the inner magnetosphere environment, and the electric fields that affect mostly low  
 120 energy particles.

121 In this coordinate system the “radial” coordinate was defined in section 1 and  
 122 is the L shell. The azimuthal coordinate is the magnetic local time (MLT). For an  
 123 observer above Earth's north pole looking down, MLT is defined to be 0 (midnight)  
 124 in the anti-sunward direction, and increases in the counter-clockwise direction with 6  
 125 at dawn, 12 at noon (sunward direction), and 18 in dusk. The final coordinate is the  
 126 magnetic latitude,  $\lambda$  which is analogous to the latitude coordinate in the spherical  
 127 coordinate system, and is defined to be 0 at the magnetic equator. This coordinate  
 128 system naturally describes the following inner magnetosphere populations.

129        The low energy particle dynamics in the inner magnetosphere are organized by  
 130   two electric fields: the co-rotation and the dawn-dusk electric fields. The co-rotation  
 131   electric field arises from the rotation of Earth's magnetic field. Since particles are  
 132   frozen on magnetic field lines and the plasma conductivity is effectively infinite, to a  
 133   non-rotating observer, Earth's rotation appears as a radial electric field that drops off  
 134   as  $\sim L^2$ . This electric field makes particles orbit around the Earth due to the  $\vec{E} \times \vec{B}$   
 135   drift. The other electric field, pointing from dawn to dusk is called the convection  
 136   electric field and is due to the Earthward transport of particles from the magnetotail  
 137   that appears as an electric field to a stationary observer (with respect to Earth). The  
 138   superposition of the co-rotation and convection electric fields results in a potential  
 139   field shown in Fig. 1.5. The shaded area in Fig. 1.5 shows the orbits on which low  
 140   energy electrons are trapped, and outside are the untrapped particles. The dynamic  
 141   topology of the shaded region in Fig. 1.5 is controlled by only the convection electric  
 142   field which is dependent on the solar wind speed and the IMF. The lowest energy  
 143   particles, that are most effected by these electric fields, make up the plasmasphere.

144        Plasmasphere The plasmasphere is a dense ( $n_e \sim 10^3/\text{cm}^3$ ), cool plasma  
 145   ( $\sim \text{eV}$ ) that extends to  $L \sim 4$  (extent is highly dependent on the solar wind and  
 146   magnetospheric conditions) and is sourced from the ionosphere. The two main  
 147   mechanisms that source the cold plasma from the ionosphere are ultraviolet ionization  
 148   by sunlight and particle precipitation. The ultraviolet ionization by sunlight is  
 149   strongly dependent on the time of day (day vs night), latitude (more ionization near  
 150   the equator). The ionization due to particle precipitation, on the other hand, is highly  
 151   dependent on magnetospheric conditions, and mostly occurs at high latitudes.

152        The outer boundary of the plasmasphere is the plasmapause which is typically  
 153   identified as a steep radial gradient in plasma density from  $\sim 10^3/\text{cm}^3$  to  $\sim 1/\text{cm}^3$ . As

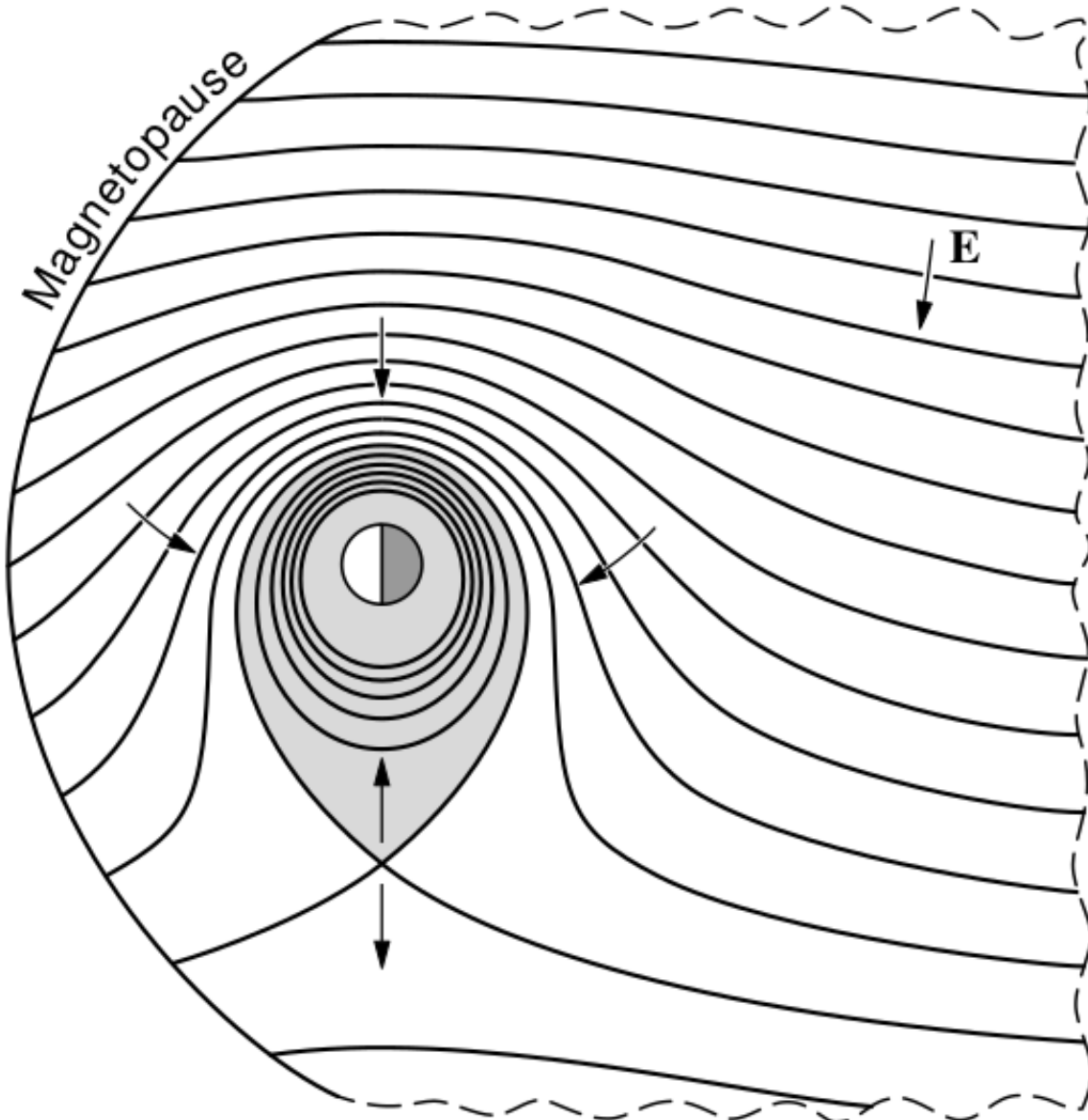


Figure 1.5: Equipotential lines and electric field arrows due to the superposition of the co-rotation and convection electric fields. Electrons in the shaded region execute closed orbits. Outside of the shaded regions the electrons are not trapped and will escape. The region separating the two regimes is called the Alfvén layer. Figure from Baumjohann and Treumann (1997).

<sub>154</sub> we will see throughout this dissertation, the location of the plasmapause is important  
<sub>155</sub> to model (e.g. O'Brien and Moldwin, 2003) and understand since the plasma density  
<sub>156</sub> strongly controls the efficiency of particle scattering (Horne et al., 2005).

<sub>157</sub> Ring Current The next higher energy population is the ring current. This  
<sub>158</sub> population consists of protons and electrons between tens and a few hundred keV  
<sub>159</sub> that drift around the Earth. The orbits of higher energy particles are not as effected  
<sub>160</sub> by the convection and co-rotation electric field, rather they drift around the Earth  
<sub>161</sub> due to gradient and curvature drifts. Since the direction of the drift is dependent on  
<sub>162</sub> charge, protons drift west around the Earth and electrons drift East. This has the  
<sub>163</sub> effect of creating a current around the Earth.

<sub>164</sub> The ring current generates a magnetic field which decreases the magnetic field  
<sub>165</sub> strength on Earth's surface and increases it outside of the ring current. The decrease  
<sub>166</sub> of Earth's magnetic field strength is readily observed by a system of ground-based  
<sub>167</sub> magnetometers and is merged into a Disturbance Storm Time (DST) index. An  
<sub>168</sub> example of a DST index time series from a coronal mass ejection (CME) driven 2015  
<sub>169</sub> St. Patrick's Day storm is shown in Fig. 1.6. The ring current is sometimes first  
<sub>170</sub> depleted and DST increases slightly (initial phase or sudden storm commencement).  
<sub>171</sub> Then the ring current is rapidly built up during which DST rapidly decreases (main  
<sub>172</sub> phase). Lastly the ring current gradually decays toward its equilibrium state over a  
<sub>173</sub> period of a few days and DST increases towards 0 (recovery phase). The DST index  
<sub>174</sub> along with other indicies are readily used by the space physics community to quantify  
<sub>175</sub> the global state of the magnetosphere.

<sub>176</sub> Radiation Belts The highest energy particle populations are in the Van Allen  
<sub>177</sub> radiation belts. These belts were discovered by Van Allen (1959) and Vernov and  
<sub>178</sub> Chudakov (1960) during the Cold War and are a pair of toroidally shaped populations

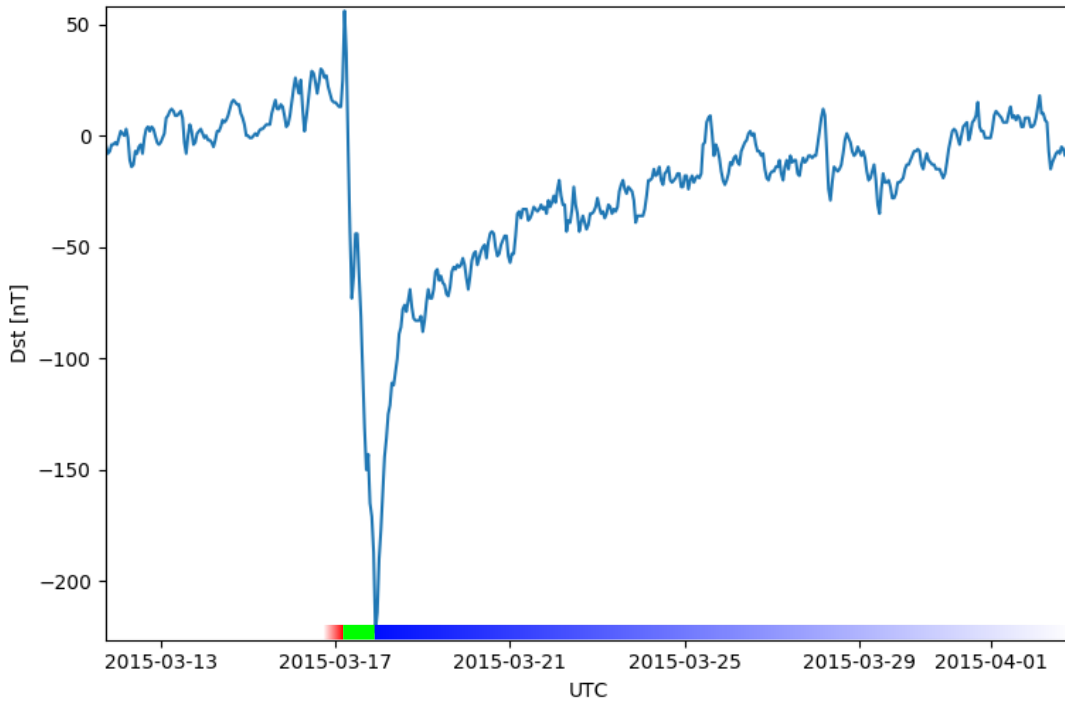


Figure 1.6: The DST index during the St. Patrick's Day 2015 storm. This storm was caused by a coronal mass ejection on March 15th, 2015. The storm phases are: initial phase, main phase, and recovery phase. The initial phase occurred when the Dst peaked at  $+50$  nT on March 17th during which the ring current was eroded by the coronal mass ejection during the interval shown by the red bar. Then the rapid decrease to  $\approx -200$  nT was during the main phase where many injections from the magnetotail pumped up the ring current which reduced Earth's magnetic field strength at the ground and is shown with the green bar. Lastly, the recovery phase lasted from March 18th to approximately March 29th during which the ring current particles were lost and the ring current returned to its equilibrium state. The recovery phase is shown with the blue bar.

## The Earth's Electron Radiation Belts

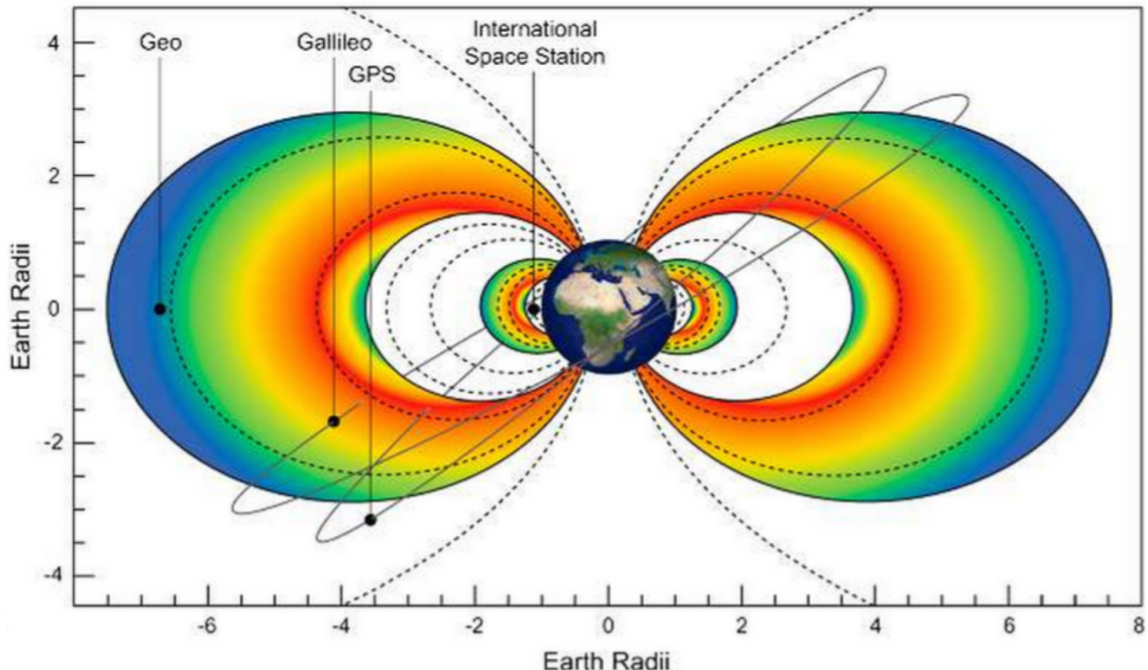


Figure 1.7: The two radiation belts with the locations of various satellites and orbits. Figure from (Horne et al., 2013).

<sup>179</sup> of trapped electrons and protons usually within to  $L < 8$  and are shown in Fig. 1.7.  
<sup>180</sup> Their quiescent toroidal shape is similar to the shape of the plasmasphere and ring  
<sup>181</sup> current and is a result of Earth's dipole magnetic field and the conservation of the  
<sup>182</sup> three adiabatic invariants discussed in section 1.

<sup>183</sup> The inner radiation belt is extremely stable on time periods of years, extends  
<sup>184</sup> to  $L \approx 2$ , and mainly consists of protons with energies between MeV and GeV and  
<sup>185</sup> electrons with energies up to  $\approx 1$  MeV (Claudepierre et al., 2019). The source of  
<sup>186</sup> inner radiation belt protons is believed to be due to cosmic-ray albedo neutron decay  
<sup>187</sup> (e.g. Li et al., 2017) and inward radial diffusion for electrons (e.g. O'Brien et al.,  
<sup>188</sup> 2016). The gap between the inner and outer radiation belt is called the slot, which is  
<sup>189</sup> believed to be due to hiss waves inside the plasmasphere (described below) scattering

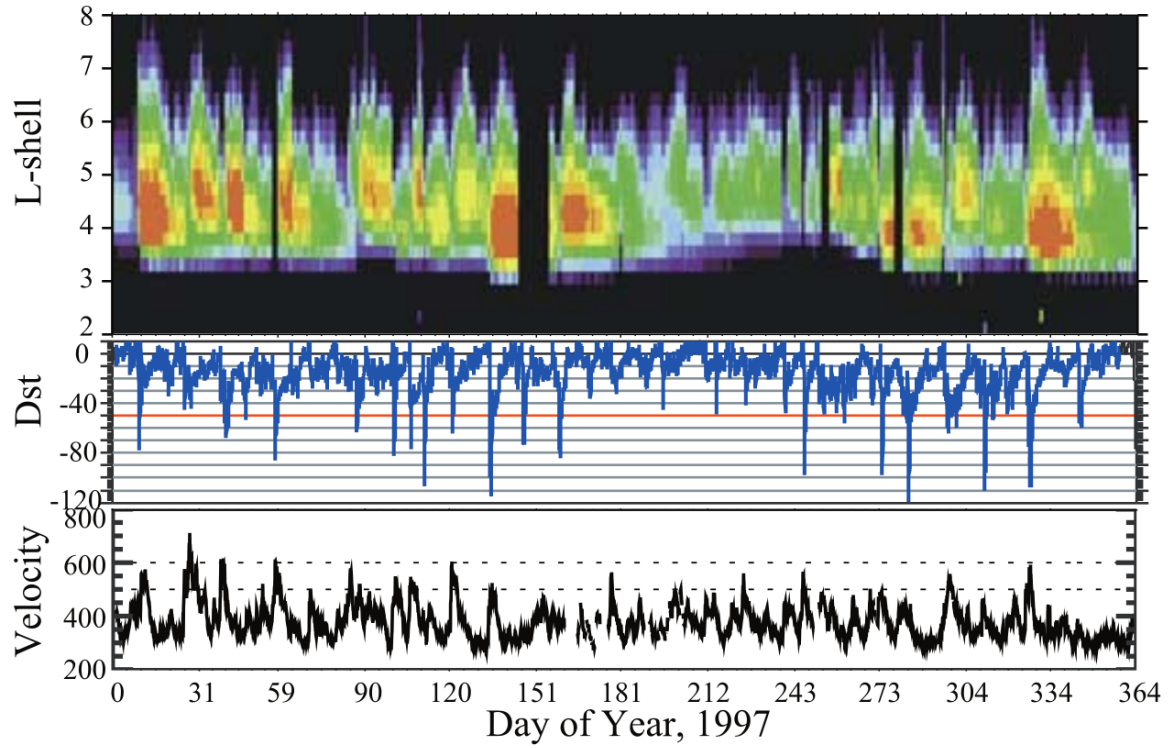


Figure 1.8: The dynamics of the outer radiation belt in 1997 from the POLAR satellite. Top panel shows the 1.2-2.4 MeV electron flux as a function of L and 1997 day of year. The middle panel shows the DST index, and bottom panel shows the solar wind velocity. Figure from (Reeves et al., 2003).

<sup>190</sup> particles into the atmosphere (e.g. Breneman et al., 2015; Lyons and Thorne, 1973).

<sup>191</sup> The outer radiation belt, on the other hand is much more dynamic and consists  
<sup>192</sup> of mainly electrons of energies up to a few MeV. The outer belt's spatial extent is  
<sup>193</sup> highly variable e.g. see Fig. 1.8, and is typically observed at  $4 < L < 8$ . Since  
<sup>194</sup> the outer radiation belt contains a dynamic population of energetic particles that  
<sup>195</sup> pose a threat to human and technological presence in Earth's atmosphere and space,  
<sup>196</sup> decades of research has been undertaken to understand and predict the outer radiation  
<sup>197</sup> belt particles, waves, and wave-particle interactions. The dynamics of the outer  
<sup>198</sup> radiation belt can be understood by considering various competing acceleration and  
<sup>199</sup> loss mechanisms which will be described in the following sections.

<sup>200</sup>

### Radiation Belt Particle Sources and Sinks

<sup>201</sup> Adiabatic Heating

<sup>202</sup> One of the particle heating and transport mechanisms arises from the Earthward  
<sup>203</sup> convection of particles. The conservation of  $J_1$  implies that the initial and final  $v_\perp$   
<sup>204</sup> depends on the change in the magnetic field amplitude

$$\frac{v_{\perp i}^2}{B_i} = \frac{v_{\perp f}^2}{B_f}. \quad (1.12)$$

<sup>205</sup> As a particle convets Earthward,  $B_f > B_i$  thus  $v_\perp$  must increase. The dipole  
<sup>206</sup> magnetic field amplitude can be written as

$$B(L, \theta) = \frac{31.2 \mu\text{T}}{L^3} \sqrt{1 + 3 \cos^2 \theta} \quad (1.13)$$

<sup>207</sup> which implies that

$$\frac{v_{\perp f}^2}{v_{\perp i}^2} = \left(\frac{L_i}{L_f}\right)^3. \quad (1.14)$$

<sup>208</sup> .

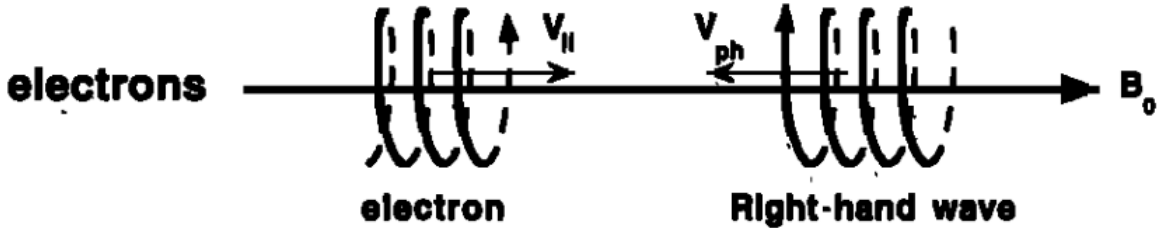
<sup>209</sup> In addition, as the particle convects Earthward the distance between the  
<sup>210</sup> particle's mirror points decrease. If  $J_2$  is conserved, the shrinking bounce path implies  
<sup>211</sup> that  $v_{||}$  must increase by

$$\frac{v_{|| f}^2}{v_{|| i}^2} = \left(\frac{L_i}{L_f}\right)^k \quad (1.15)$$

<sup>212</sup> where  $k$  ranges from 2 for equatorial pitch angles,  $\alpha_{eq} = 0^\circ$ , to 2.5 for  $\alpha_{eq} = 90^\circ$   
<sup>213</sup> (Baumjohann and Treumann, 1997). Since the rate of adiabatic heating is greater in  
<sup>214</sup> the perpendicular direction than heating in the parallel direction, an initially isotropic  
<sup>215</sup> particle distribution will become anisotropic during its convection. These isotropic  
<sup>216</sup> particles can then become unstable to wave growth and generate waves in order to  
<sup>217</sup> reach equilibrium.

<sup>218</sup> Wave Resonance Heating

<sup>219</sup> Another mechanism that heats particles is due to particles resonating with  
<sup>220</sup> plasma waves. A few of the electromagnetic wave modes responsible for particle  
<sup>221</sup> acceleration (and deceleration) relevant to radiation belt dynamics are hiss, whistler  
<sup>222</sup> mode chorus (chorus), and electromagnetic ion cyclotron (EMIC) waves. These waves  
<sup>223</sup> are created by the loss cone instability that driven by an anisotropy of electrons  
<sup>224</sup> for chorus waves, and protons for EMIC waves. The level of anisotropy can be  
<sup>225</sup> quantified by the ratio of the perpendicular to parallel particle temperatures ( $T_{\perp}/T_{||}$ ).  
<sup>226</sup> A particle distribution is unstable when  $T_{\perp}/T_{||} > 1$  which facilitates wave growth.



$$\omega + k_{\parallel} v_{\parallel} = \Omega^-$$

Figure 1.9: The trajectories of an electron and a right-hand circularly polarized wave during a cyclotron resonance. The electron's  $v_{\parallel}$  and the wave's  $k_{\parallel}$  are in opposite directions such that the wave's frequency is Doppler shifted to an integer multiple of the electron cyclotron frequency. Figure from (Tsurutani and Lakhina, 1997).

227 Since electrons gyrate in a right-handed sense, the chorus waves also tend to be right  
 228 hand circularly polarized (Tsurutani and Lakhina, 1997). The same argument applies  
 229 to protons and left hand circularly polarized EMIC waves as well.

230 These circularly polarized waves can resonate with electrons and/or protons  
 231 when their combined motion results in a static  $\vec{E}$ . One example of a resonance  
 232 between a right hand circularly polarized wave and an electron is shown in Fig. 1.21  
 233 and is termed the cyclotron resonance. An electron's  $v_{\parallel}$  and the wave's parallel wave  
 234 vector,  $k_{\parallel}$  are in opposite directions such that the wave frequency  $\omega$  is Doppler shifted  
 235 to an integer multiple of the  $\Omega_e$  at which point the electron feels a static electric  
 236 field and is accelerated or decelerated. This acceleration happens when a resonance  
 237 condition is satisfied between a wave and a particle for which we will now derive an  
 238 illustrative toy model.

239 Assume a uniform magnetic field  $\vec{B} = B_0 \hat{z}$  with a parallel propagating ( $k = k\hat{z}$ ),  
 240 right-hand circularly polarized wave. The wave's electric field as a function of position  
 241 and time can be written as

$$\vec{E} = E_0 (\cos(\omega t - kz) \hat{x} + \sin(\omega t - kz) \hat{y}) \quad (1.16)$$

which is more clearly expressed by taking the dot product to find  $\vec{E}$  in the  $\hat{\theta}$  direction

$$E_\theta = \vec{E} \times \hat{\theta} = E_0 \cos(\omega t - kz + \theta). \quad (1.17)$$

<sup>242</sup> Now assume that the electron is traveling in the  $-\hat{z}$  direction with a velocity  $\vec{v} = -v_0 \hat{z}$   
<sup>243</sup> so its time dependent position along  $\hat{z}$  is

$$z(t) = -v_0 t \quad (1.18)$$

<sup>244</sup> and gyrophase is

$$\theta(t) = -\Omega t + \theta(0) \quad (1.19)$$

<sup>245</sup> where the first negative sign comes from the electron's negative charge. Now we put  
<sup>246</sup> this all together and express the electric field and the force that the electron will  
<sup>247</sup> experience

$$m \frac{dv_\theta}{dt} = qE_\theta = qE_0 \sin((\omega + kv_0 - \Omega)t + \theta(0)). \quad (1.20)$$

<sup>248</sup> This is a relatively complex expression, but when the time dependent component,

$$\omega + kv_0 - \Omega = 0, \quad (1.21)$$

<sup>249</sup> the electron will be in a static electric field which will accelerate or decelerate the  
<sup>250</sup> electron depending on  $\theta_0$ , the phase between the wave and the electron. **Show Bortnik  
<sup>251</sup> 2008 plot?** The expression in Eq. 1.21 is commonly referred to as the resonance

252 condition and is more generally written as

$$\omega - k_{||}v_{||} = \frac{n\Omega_e}{\gamma} \quad (1.22)$$

253 where  $n$  is the resonance order, and  $\gamma$  is the relativistic correction (e.g. Millan and  
254 Thorne, 2007). In the case of the cyclotron resonance,  $\omega \approx \Omega_e$  thus  $J_1$  is violated.  
255 Since  $J_1$  is violated,  $J_2$  and  $J_3$  are also violated since the conditions required to  
256 violate  $J_2$  and  $J_3$  are less stringent than  $J_1$ . It is important to remember that along  
257 the particle's orbit it will encounter and experience the effects of many waves along  
258 its orbit. The typical MLT extent of a handful of waves that are capable of resonating  
259 with radiation belt electrons are shown in Fig. 1.10.

260 Particle Losses

261 Now that we have seen two general mechanisms with which particles are  
262 accelerated and transported in the magnetosphere, we will now consider a few  
263 specific mechanisms with which particles are lost to the atmosphere or the solar  
264 wind. One particle loss mechanism into the solar wind is magnetopause shadowing  
265 (e.g. Ukhorskiy et al., 2006). Particles are sometimes lost when the ring current is  
266 strengthened and Earth's magnetic field strength is increased outside of the ring  
267 current (and reduced on Earth's surface). If the time scale of the ring current  
268 strengthening is slower than a particle drift,  $J_3$  is conserved. Then in order to  
269 conserve  $J_3$  while the magnetic field strength is increased, the particle's drift shell  
270 must move outward to conserve the magnetic flux contained by the drift shell. Then  
271 if the particle's drift shell expands to the point that it crosses the magnetopause, the  
272 particle will be lost to the solar wind.

273 **Move to acceleration?** Another particle loss and acceleration mechanism is driven  
274 by ultra low frequency (ULF) waves and is called radial diffusion. Radial diffusion is

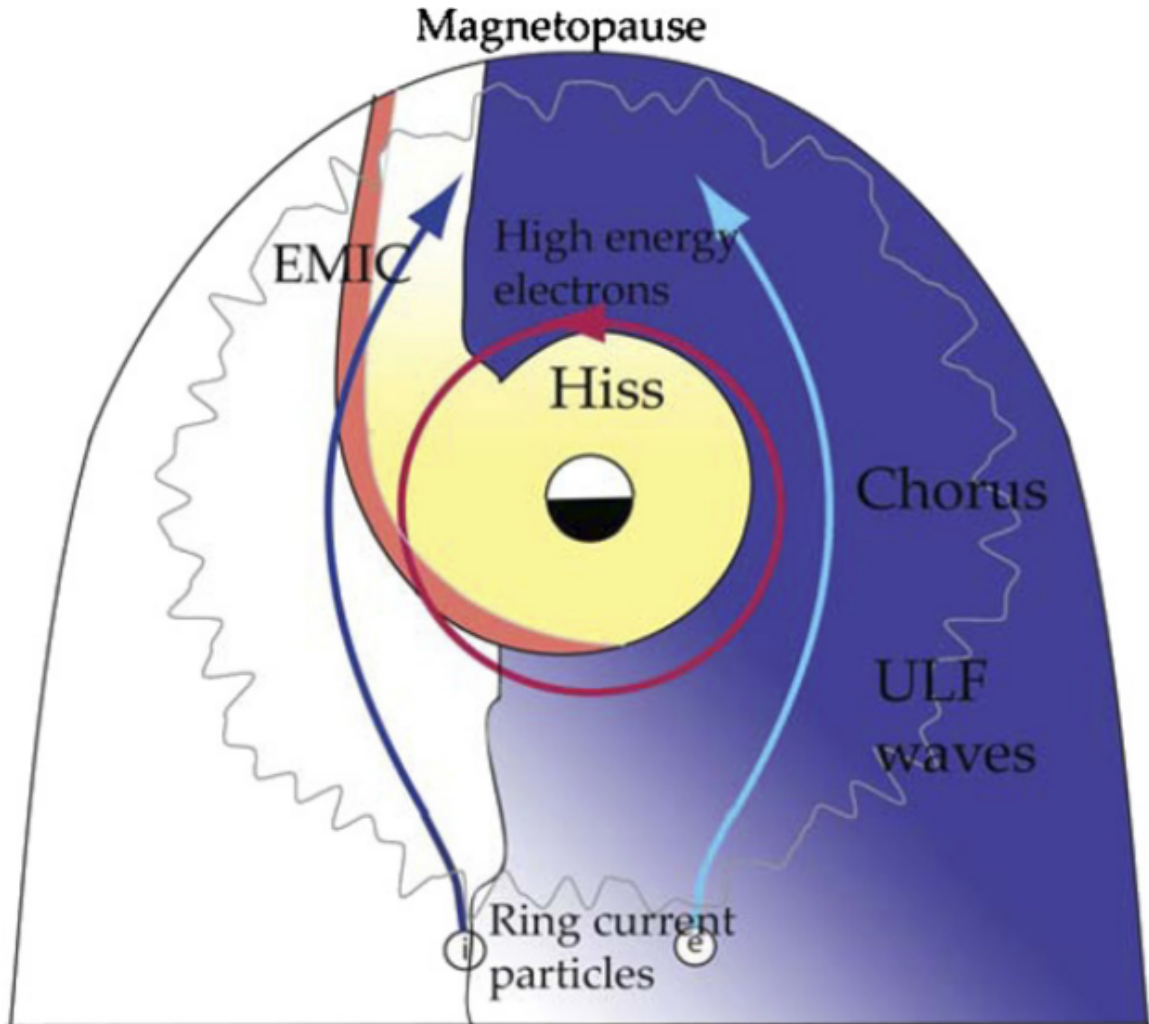


Figure 1.10: Various wave modes in the magnetosphere. Ultra low frequency waves occur through the magnetosphere. Chorus waves are typically observed in the 0-12 midnight-dawn region. EMIC waves are typically observed in the dusk MLT sector. Hiss waves are observed inside the plasmasphere. Figure from Millan and Thorne (2007).

275 the transport of particles from high to low phase space density,  $f$ . If the transport is  
 276 radially inward, particles will appear to be accelerated. On the other hand, radially  
 277 outward radial diffusion can transport particles through the magnetopause where  
 278 they will be lost to the solar wind. Reeves et al. (2013) investigated the driver of  
 279 particle acceleration during the October 2012 storm and observationally found that  
 280 inward radial diffusion was not dominant, rather local acceleration via wave-resonance  
 281 heating (i.e. particle diffusion in pitch angle and energy which will be described below)  
 282 appeared to be the dominant acceleration mechanism.

283 The loss mechanism central to this dissertation is pitch angle and energy  
 284 scattering of electrons by waves. Some of the waves that scatter electrons in energy  
 285 and pitch angle in the inner magnetosphere are: plasmaspheric hiss (e.g. Breneman  
 286 et al., 2015; O'Brien et al., 2014), EMIC waves (e.g. Capannolo et al., 2019; Hendry  
 287 et al., 2017), and chorus waves (e.g. Breneman et al., 2017; Kasahara et al., 2018;  
 288 Ozaki et al., 2019). These wave-particle interactions occur when the resonance  
 289 condition in Eq. 1.22 is satisfied at which point the particle's energy and  $\alpha$  is modified  
 290 by the wave. More details regarding the theory of pitch angle and energy diffusion is  
 291 given in Chapter X. If the wave changes  $\alpha$  towards 0 such that  $\alpha < \alpha_{LC}$ , the particle's  
 292 mirror point lowers to less than 100 km altitude where the particle can be lost due  
 293 collisions with air. One manifestation of pitch angle scattering of particles into the  
 294 loss cone are microbursts: a sub-second duraion impulse of electrons.

295

### Microbursts

296 Microbursts were first found in high altitude balloon measurements of bremsstrahlung  
 297 X-rays emitted by microburst electrons impacting the atmosphere by Anderson  
 298 and Milton (1964). In the following years, numerous balloon flights expanded our  
 299 knowledge of non-relativistic microbursts (relativistic microbursts have not yet been

300 observed by high altitude balloons) by quantifying the microburst spatial extent,  
 301 temporal width, occurrence frequency, extent in L and MLT, and their source (a  
 302 local plasma instability vs. a propagating disturbance in the magnetosphere) (e.g.  
 303 Barcus et al., 1966; Brown et al., 1965; Parks, 1967; Trefall et al., 1966). Since then,  
 304 non-relativistic and relativistic ( $> 500$  keV) microbursts electrons have been directly  
 305 observed in LEO with spacecraft including the Solar Anomalous and Magnetospheric  
 306 Particle Explorer (SAMPEX) (e.g. Blake et al., 1996; Blum et al., 2015; Douma et al.,  
 307 2019, 2017; Greeley et al., 2019; Lorentzen et al., 2001a,b; Nakamura et al., 1995, 2000;  
 308 O'Brien et al., 2004, 2003), Montana State University's (MSU) Focused Investigation  
 309 of Relativistic Electron Bursts: Intensity, Range, and Dynamics II (FIREBIRD-II)  
 310 (Anderson et al., 2017; Breneman et al., 2017; Crew et al., 2016; Klumpar et al.,  
 311 2015; Spence et al., 2012), and Science Technologies Satellite (STSAT-I) (e.g. Lee  
 312 et al., 2012, 2005). An example microburst time series is shown in Fig. 1.11 and was  
 313 observed by the FIREBIRD-II CubeSats. The prominent features of the example  
 314 microbursts in Fig. 1.11 are their  $< 1$  second duration, half order of magnitude  
 315 increase in count rate above the falling background, and their approximately 200-800  
 316 keV energy extent.

317 Microbursts are observed on magnetic field footprints that are connected to the  
 318 outer radiation belt (approximately  $4 < L < 8$ ), and are predominately observed in  
 319 the 0-12 MLT sector with an elevated occurrence frequency during magnetospherically  
 320 disturbed times as shown in Fig. 1.12 (e.g. Douma et al., 2017). O'Brien et al. (2003)  
 321 used SAMPEX relativistic electron data and found that microbursts predominately  
 322 occur during the main phase of storms, with a heightened occurrence rate during the  
 323 recovery phase. Microburst occurrence rates also appear to be higher during high  
 324 solar wind velocity events e.g. from co-rotating interaction regions (Greeley et al.,  
 325 2019; O'Brien et al., 2003).

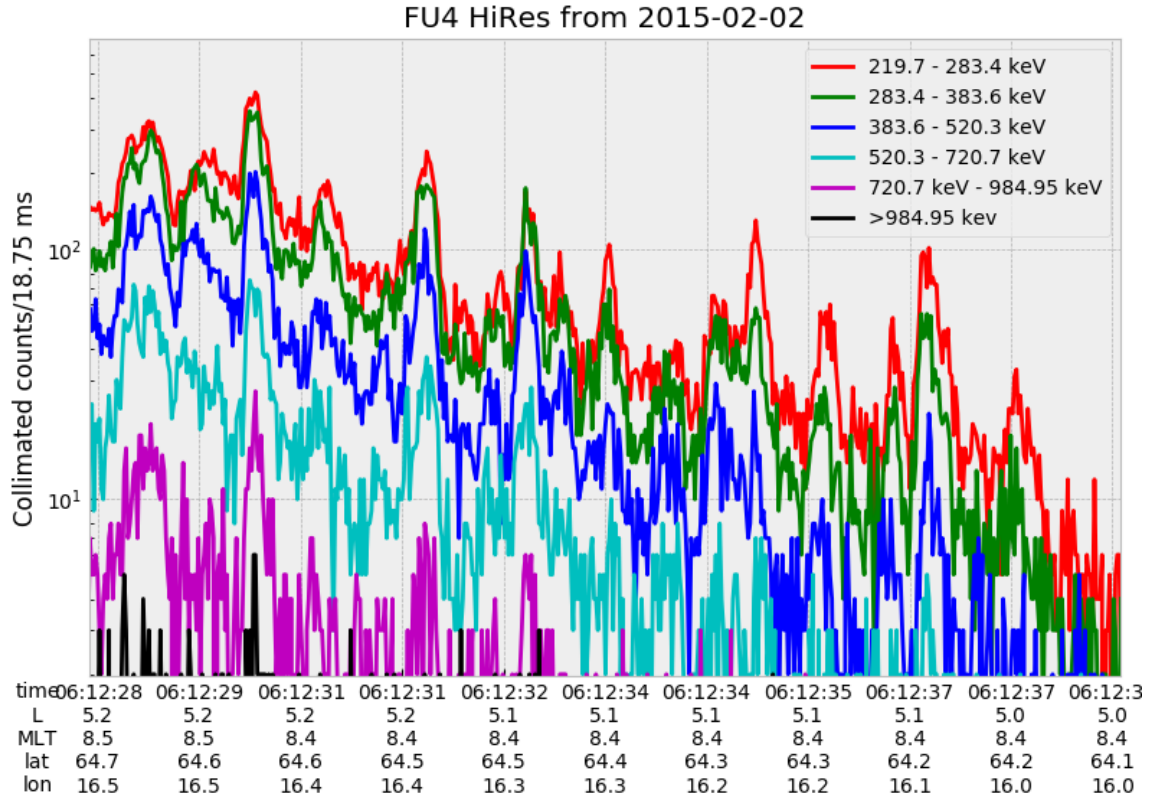


Figure 1.11: An example train of microbursts observed by FIREBIRD-II unit 4 on February 2nd, 2015. The colored curves show the differential energy channel count rates in six channels from  $\approx 200$  keV to greater than 1 MeV. The x-axis labels show auxiliary information such as time of observation and the spacecraft position in L, MLT, latitude and longitude coordinates.

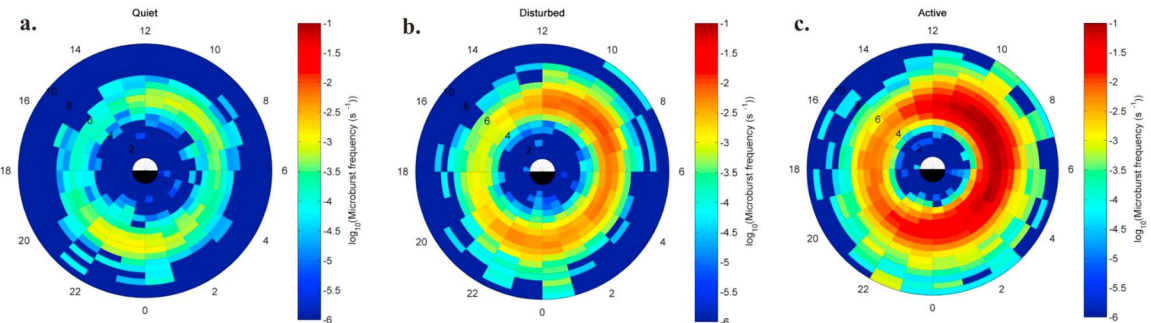


Figure 1.12: Relativistic ( $> 1\text{MeV}$ ) distribution of microburst occurrence rates as a function of L and MLT. The three panels show the microburst occurrence rate dependence on geomagnetic activity, parameterized by the auroral electrojet (AE) index for (a)  $\text{AE} < 100 \text{nT}$ , (b)  $100 < \text{AE} < 300 \text{nT}$  and (c)  $\text{AE} > 300 \text{nT}$ . Figure from Douma et al. (2017).

326        The impact of microbursts on atmospheric chemistry has been estimated to be  
 327        significant. Relativistic microburst electrons impacting the atmosphere are ionized at  
 328         $< 100 \text{ km}$  altitudes, with higher energy electrons penetrating closer to the surface.  
 329        The resulting chemical reaction of microburst electrons impacting the atmosphere  
 330        produces odd hydrogen  $\text{HO}_x$  and odd nitrogen  $\text{NO}_x$  molecules. These molecules are  
 331        partially responsible for destroying ozone ( $\text{O}_3$ ). Seppälä et al. (2018) modeled a six  
 332        hour relativistic microburst storm and found that the mesospheric ozone was reduced  
 333        by 7 – 12% in the summer months and 12 – 20% in the winter months.

334        Furthermore, microbursts have also been estimated to have a significant impact  
 335        on the outer radiation belt electrons. Radiation belt electron loss due to microbursts  
 336        has been estimated to be on the order of a day (Breneman et al., 2017; Douma  
 337        et al., 2019; Lorentzen et al., 2001b; O'Brien et al., 2004; Thorne et al., 2005).

338        The wave-particle interactions responsible for generating microbursts are also  
 339        believed to accelerate electrons in the radiation belts. **Mention Thorne's and Paul's  
 340        work on microburst acceleration and losses**

341        The range of observed microburst energies range from a few tens of keV (e.g.

<sup>342</sup> Datta et al., 1997; Parks, 1967) to greater than 1 MeV (e.g. Blake et al., 1996; Greeley  
<sup>343</sup> et al., 2019). The microburst electron flux ( $J$ ) falls off in energy, and the microburst  
<sup>344</sup> energy spectra is typically well fit to a decaying exponential

$$J(E) = J_0 e^{-E/E_0} \quad (1.23)$$

<sup>345</sup> where  $J_0$  is the flux at 0 keV (unphysical free parameter) and  $E_0$  quantifies the  
<sup>346</sup> efficiency of the scattering mechanism in energy (.e.g Datta et al., 1997; Lee et al.,  
<sup>347</sup> 2005; Parks, 1967). A small  $E_0$  suggests that mostly low energy particles are scattered  
<sup>348</sup> and a high  $E_0$  suggests that the scattering mechanism scatters low and high energy  
<sup>349</sup> electrons. Reality is a bit more messy and a high  $E_0$  may be a signature of a scattering  
<sup>350</sup> mechanism preferential to high energy electrons, but is hidden by the convolution of  
<sup>351</sup> the source particles available to be scattered (typically with a falling energy spectrum)  
<sup>352</sup> and the energy-dependent scattering efficiency.

<sup>353</sup> The short duration of microbursts observed by a single LEO satellite has an  
<sup>354</sup> ambiguity when interpreting what is exactly a microburst. The two possible realities  
<sup>355</sup> are: a microburst is very small and spatially stationary so that the LEO spacecraft  
<sup>356</sup> passes through it in less than a second. Alternatively, microbursts are spatially large  
<sup>357</sup> with a short duration such that the microburst passes by the spacecraft in a fraction  
<sup>358</sup> of a second. There are a few ways to distinguish between the two possible realities,  
<sup>359</sup> and each one has a unique set of advantages.

<sup>360</sup> A high altitude balloon provides essentially a stationary view of the precipitating  
<sup>361</sup> particles under the radiation belt footprints so a short-lived, temporal microburst  
<sup>362</sup> can be unambiguously identified. Spatial structures on the other hand are difficult  
<sup>363</sup> to identify because a balloon is essentially still on drift timescales thus a variation in  
<sup>364</sup> the X-rays can be due to the spatial structure or an increase of precipitating particles

365 over the whole area. Furthermore, if the stationary structure is drifting its particles  
 366 are not precipitating into the atmosphere so there is no X-ray signature.

367 Another solution is multi-spacecraft missions that can determine if a microburst  
 368 is spatial or temporal. As will be shown in this dissertation, if a microburst is  
 369 observed simultaneously by two spacecraft then it is temporally transient and has  
 370 a size greater than the spacecraft separation. On the other hand, if two spacecraft  
 371 observe a microburst-like feature in the same location and at different times, then it is  
 372 spatial may be a curtain (Blake and O'Brien, 2016). Both observational methods have  
 373 a unique set of strengths, and this dissertation takes the multi-spacecraft approach  
 374 to identify and study microbursts.

375

### Scope of Reserach

376 This dissertation furthers our understanding of the microburst scattering  
 377 mechanism by observing the scattering directly, and measuring the microburst sizes  
 378 and comparing them to the size of waves near the magnetic equator where those  
 379 electrons could have been scattered. Chapter X describes a microburst scattering  
 380 event observed by NASA's Van Allen Probes which was studied in the theoretic  
 381 framework of pitch angle and energy diffusion. The following two chapters will then  
 382 study the size of microbursts. Chapter Y describes a bouncing packet microburst  
 383 observation made by MSU's FIREBIRD-II mission where the microburst's lower  
 384 bound longitudinal and latitudinal sizes were estimated. Then Chapter Z expands  
 385 the case study from Ch. Y to a statistical study of microburst sizes using The  
 386 Aerospace Corporation's AeroCube-6 (AC6) CubeSats. In this study, a Monte Carlo  
 387 and analytic microburst size models were developed to account for the compounding  
 388 effects of random microburst sizes and locations. Lastly, Ch. A will summarize the  
 389 dissertation work and make concluding remarks regarding outstanding questions in

<sup>390</sup> microburst physics.

## Bibliography

- 392 Anderson, B., Shekhar, S., Millan, R., Crew, A., Spence, H., Klumpar, D., Blake, J.,  
 393 O'Brien, T., and Turner, D. (2017). Spatial scale and duration of one microburst  
 394 region on 13 August 2015. *Journal of Geophysical Research: Space Physics*.
- 395 Anderson, K. A. and Milton, D. W. (1964). Balloon observations of X rays in the  
 396 auroral zone: 3. High time resolution studies. *Journal of Geophysical Research*,  
 397 69(21):4457–4479.
- 398 Barcus, J., Brown, R., and Rosenberg, T. (1966). Spatial and temporal character of  
 399 fast variations in auroral-zone x rays. *Journal of Geophysical Research*, 71(1):125–  
 400 141.
- 401 Baumjohann, W. and Treumann, R. A. (1997). *Basic space plasma physics*. World  
 402 Scientific.
- 403 Blake, J.,Looper, M., Baker, D., Nakamura, R., Klecker, B., and Hovestadt, D.  
 404 (1996). New high temporal and spatial resolution measurements by sampex of the  
 405 precipitation of relativistic electrons. *Advances in Space Research*, 18(8):171 – 186.
- 406 Blake, J. B. and O'Brien, T. P. (2016). Observations of small-scale latitudinal  
 407 structure in energetic electron precipitation. *Journal of Geophysical Research: Space  
 408 Physics*, 121(4):3031–3035. 2015JA021815.
- 409 Blum, L., Li, X., and Denton, M. (2015). Rapid MeV electron precipitation as  
 410 observed by SAMPEX/HILT during high-speed stream-driven storms. *Journal of  
 411 Geophysical Research: Space Physics*, 120(5):3783–3794. 2014JA020633.
- 412 Breneman, A., Crew, A., Sample, J., Klumpar, D., Johnson, A., Agapitov, O.,  
 413 Shumko, M., Turner, D., Santolik, O., Wygant, J., et al. (2017). Observations  
 414 directly linking relativistic electron microbursts to whistler mode chorus: Van allen  
 415 probes and FIREBIRD II. *Geophysical Research Letters*.
- 416 Breneman, A. W., Halford, A., Millan, R., McCarthy, M., Fennell, J., Sample, J.,  
 417 Woodger, L., Hospodarsky, G., Wygant, J. R., Cattell, C. A., et al. (2015). Global-  
 418 scale coherence modulation of radiation-belt electron loss from plasmaspheric hiss.  
 419 *Nature*, 523(7559):193.
- 420 Brown, R., Barcus, J., and Parsons, N. (1965). Balloon observations of auroral zone  
 421 x rays in conjugate regions. 2. microbursts and pulsations. *Journal of Geophysical  
 422 Research (U.S.)*.
- 423 Capannolo, L., Li, W., Ma, Q., Shen, X.-C., Zhang, X.-J., Redmon, R., Rodriguez,  
 424 J., Engebretson, M., Kletzing, C., Kurth, W., et al. (2019). Energetic electron  
 425 precipitation: multi-event analysis of its spatial extent during emic wave activity.  
 426 *Journal of Geophysical Research: Space Physics*.

- 427 Claudepierre, S., O'Brien, T.,Looper, M., Blake, J., Fennell, J., Roeder, J.,  
 428 Clemmons, J., Mazur, J., Turner, D., Reeves, G., et al. (2019). A revised look  
 429 at relativistic electrons in the earth's inner radiation zone and slot region. *Journal*  
 430 *of Geophysical Research: Space Physics*, 124(2):934–951.
- 431 Crew, A. B., Spence, H. E., Blake, J. B., Klumpar, D. M., Larsen, B. A., O'Brien,  
 432 T. P., Driscoll, S., Handley, M., Legere, J., Longworth, S., Mashburn, K.,  
 433 Mosleh, E., Ryhajlo, N., Smith, S., Springer, L., and Widholm, M. (2016). First  
 434 multipoint in situ observations of electron microbursts: Initial results from the  
 435 NSF FIREBIRD II mission. *Journal of Geophysical Research: Space Physics*,  
 436 121(6):5272–5283. 2016JA022485.
- 437 Datta, S., Skoug, R., McCarthy, M., and Parks, G. (1997). Modeling of microburst  
 438 electron precipitation using pitch angle diffusion theory. *Journal of Geophysical*  
 439 *Research: Space Physics*, 102(A8):17325–17333.
- 440 Douma, E., Rodger, C., Blum, L., O'Brien, T., Clilverd, M., and Blake, J. (2019).  
 441 Characteristics of relativistic microburst intensity from sampex observations.  
 442 *Journal of Geophysical Research: Space Physics*.
- 443 Douma, E., Rodger, C. J., Blum, L. W., and Clilverd, M. A. (2017). Occurrence  
 444 characteristics of relativistic electron microbursts from SAMPEX observations.  
 445 *Journal of Geophysical Research: Space Physics*, 122(8):8096–8107. 2017JA024067.
- 446 Eastwood, J., Hietala, H., Toth, G., Phan, T., and Fujimoto, M. (2015). What  
 447 controls the structure and dynamics of earths magnetosphere? *Space Science*  
 448 *Reviews*, 188(1-4):251–286.
- 449 Greeley, A., Kanekal, S., Baker, D., Klecker, B., and Schiller, Q. (2019). Quantifying  
 450 the contribution of microbursts to global electron loss in the radiation belts. *Journal*  
 451 *of Geophysical Research: Space Physics*.
- 452 Hendry, A. T., Rodger, C. J., and Clilverd, M. A. (2017). Evidence of sub-mev  
 453 emic-driven electron precipitation. *Geophysical Research Letters*, 44(3):1210–1218.
- 454 Horne, R., Glauert, S., Meredith, N., Boscher, D., Maget, V., Heynderickx, D., and  
 455 Pitchford, D. (2013). Space weather impacts on satellites and forecasting the earth's  
 456 electron radiation belts with spacecast. *Space Weather*, 11(4):169–186.
- 457 Horne, R. B., Thorne, R. M., Shprits, Y. Y., Meredith, N. P., Glauert, S. A., Smith,  
 458 A. J., Kanekal, S. G., Baker, D. N., Engebretson, M. J., Posch, J. L., et al.  
 459 (2005). Wave acceleration of electrons in the van allen radiation belts. *Nature*,  
 460 437(7056):227.
- 461 Kasahara, S., Miyoshi, Y., Yokota, S., Mitani, T., Kasahara, Y., Matsuda, S.,  
 462 Kumamoto, A., Matsuoka, A., Kazama, Y., Frey, H., et al. (2018). Pulsating  
 463 aurora from electron scattering by chorus waves. *Nature*, 554(7692):337.

- 464 Klumpar, D., Springer, L., Mosleh, E., Mashburn, K., Berardinelli, S., Gunderson,  
 465 A., Handly, M., Ryhajlo, N., Spence, H., Smith, S., Legere, J., Widholm, M.,  
 466 Longworth, S., Crew, A., Larsen, B., Blake, J., and Walmsley, N. (2015). Flight  
 467 system technologies enabling the twin-cubesat firebird-ii scientific mission.
- 468 Lee, J. J., Parks, G. K., Lee, E., Tsurutani, B. T., Hwang, J., Cho, K. S., Kim, K.-H.,  
 469 Park, Y. D., Min, K. W., and McCarthy, M. P. (2012). Anisotropic pitch angle  
 470 distribution of 100 keV microburst electrons in the loss cone: measurements from  
 471 STSAT-1. *Annales Geophysicae*, 30(11):1567–1573.
- 472 Lee, J.-J., Parks, G. K., Min, K. W., Kim, H. J., Park, J., Hwang, J., McCarthy,  
 473 M. P., Lee, E., Ryu, K. S., Lim, J. T., Sim, E. S., Lee, H. W., Kang, K. I., and  
 474 Park, H. Y. (2005). Energy spectra of 170–360 keV electron microbursts measured  
 475 by the korean STSAT-1. *Geophysical Research Letters*, 32(13). L13106.
- 476 Li, X., Selesnick, R., Schiller, Q., Zhang, K., Zhao, H., Baker, D. N., and Temerin,  
 477 M. A. (2017). Measurement of electrons from albedo neutron decay and neutron  
 478 density in near-earth space. *Nature*, 552(7685):382.
- 479 Lorentzen, K. R., Blake, J. B., Inan, U. S., and Bortnik, J. (2001a). Observations  
 480 of relativistic electron microbursts in association with VLF chorus. *Journal of  
 481 Geophysical Research: Space Physics*, 106(A4):6017–6027.
- 482 Lorentzen, K. R.,Looper, M. D., and Blake, J. B. (2001b). Relativistic electron  
 483 microbursts during the GEM storms. *Geophysical Research Letters*, 28(13):2573–  
 484 2576.
- 485 Lyons, L. R. and Thorne, R. M. (1973). Equilibrium structure of radiation belt  
 486 electrons. *Journal of Geophysical Research*, 78(13):2142–2149.
- 487 Millan, R. and Thorne, R. (2007). Review of radiation belt relativistic electron losses.  
 488 *Journal of Atmospheric and Solar-Terrestrial Physics*, 69(3):362 – 377.
- 489 Nakamura, R., Baker, D. N., Blake, J. B., Kanekal, S., Klecker, B., and Hovestadt,  
 490 D. (1995). Relativistic electron precipitation enhancements near the outer edge of  
 491 the radiation belt. *Geophysical Research Letters*, 22(9):1129–1132.
- 492 Nakamura, R., Isowa, M., Kamide, Y., Baker, D., Blake, J., and Looper, M. (2000).  
 493 Observations of relativistic electron microbursts in association with VLF chorus.  
 494 *J. Geophys. Res.*, 105:15875–15885.
- 495 O'Brien, T., Claudepierre, S., Blake, J., Fennell, J. F., Clemons, J., Roeder, J.,  
 496 Spence, H. E., Reeves, G., and Baker, D. (2014). An empirically observed pitch-  
 497 angle diffusion eigenmode in the earth's electron belt near  $l^* = 5.0$ . *Geophysical  
 498 Research Letters*, 41(2):251–258.

- 499 O'Brien, T., Claudepierre, S., Guild, T., Fennell, J., Turner, D., Blake, J., Clemmons,  
 500 J., and Roeder, J. (2016). Inner zone and slot electron radial diffusion revisited.  
 501 *Geophysical Research Letters*, 43(14):7301–7310.
- 502 O'Brien, T. and Moldwin, M. (2003). Empirical plasmapause models from magnetic  
 503 indices. *Geophysical Research Letters*, 30(4).
- 504 O'Brien, T. P., Looper, M. D., and Blake, J. B. (2004). Quantification of relativistic  
 505 electron microburst losses during the GEM storms. *Geophysical Research Letters*,  
 506 31(4). L04802.
- 507 O'Brien, T. P., Lorentzen, K. R., Mann, I. R., Meredith, N. P., Blake, J. B., Fennell,  
 508 J. F., Looper, M. D., Milling, D. K., and Anderson, R. R. (2003). Energization of  
 509 relativistic electrons in the presence of ULF power and MeV microbursts: Evidence  
 510 for dual ULF and VLF acceleration. *Journal of Geophysical Research: Space  
 511 Physics*, 108(A8).
- 512 Ozaki, M., Miyoshi, Y., Shiokawa, K., Hosokawa, K., Oyama, S.-i., Kataoka, R.,  
 513 Ebihara, Y., Ogawa, Y., Kasahara, Y., Yagitani, S., et al. (2019). Visualization of  
 514 rapid electron precipitation via chorus element wave–particle interactions. *Nature  
 515 communications*, 10(1):257.
- 516 Parks, G. K. (1967). Spatial characteristics of auroral-zone X-ray microbursts. *Journal  
 517 of Geophysical Research*, 72(1):215–226.
- 518 Reeves, G., Spence, H. E., Henderson, M., Morley, S., Friedel, R., Funsten, H., Baker,  
 519 D., Kanekal, S., Blake, J., Fennell, J., et al. (2013). Electron acceleration in the  
 520 heart of the van allen radiation belts. *Science*, 341(6149):991–994.
- 521 Reeves, G. D., McAdams, K. L., Friedel, R. H. W., and O'Brien, T. P. (2003). Ac-  
 522 celeration and loss of relativistic electrons during geomagnetic storms. *Geophysical  
 523 Research Letters*, 30(10):n/a–n/a. 1529.
- 524 Schulz, M. and Lanzerotti, L. J. (1974). *Particle Diffusion in the Radiation Belts*.  
 525 Springer.
- 526 Seppälä, A., Douma, E., Rodger, C., Verronen, P., Clilverd, M. A., and Bortnik, J.  
 527 (2018). Relativistic electron microburst events: Modeling the atmospheric impact.  
 528 *Geophysical Research Letters*, 45(2):1141–1147.
- 529 Spence, H. E., Blake, J. B., Crew, A. B., Driscoll, S., Klumpar, D. M., Larsen,  
 530 B. A., Legere, J., Longworth, S., Mosleh, E., O'Brien, T. P., Smith, S., Springer,  
 531 L., and Widholm, M. (2012). Focusing on size and energy dependence of electron  
 532 microbursts from the van allen radiation belts. *Space Weather*, 10(11).

- 533 Thorne, R. M., O'Brien, T. P., Shprits, Y. Y., Summers, D., and Horne, R. B. (2005).  
534 Timescale for MeV electron microburst loss during geomagnetic storms. *Journal*  
535 *of Geophysical Research: Space Physics*, 110(A9). A09202.
- 536 Trefall, H., Bjordal, J., Ullaland, S., and Stadsnes, J. (1966). On the extension of  
537 auroral-zone x-ray microbursts. *Journal of Atmospheric and Terrestrial Physics*,  
538 28(2):225–233.
- 539 Tsurutani, B. T. and Lakhina, G. S. (1997). Some basic concepts of wave-particle  
540 interactions in collisionless plasmas. *Reviews of Geophysics*, 35(4):491–501.
- 541 Ukhorskiy, A. Y., Anderson, B. J., Brandt, P. C., and Tsyganenko, N. A. (2006).  
542 Storm time evolution of the outer radiation belt: Transport and losses. *Journal of*  
543 *Geophysical Research: Space Physics*, 111(A11):n/a–n/a. A11S03.
- 544 Van Allen, J. A. (1959). The geomagnetically trapped corpuscular radiation. *Journal*  
545 *of Geophysical Research*, 64(11):1683–1689.
- 546 Vernov, S. and Chudakov, A. (1960). Investigation of radiation in outer space. In  
547 *International Cosmic Ray Conference*, volume 3, page 19.